



DIGITAL ACCESS TO
SCHOLARSHIP AT HARVARD
DASH.HARVARD.EDU



HARVARD LIBRARY
Office for Scholarly Communication

Amplifying the response of soft actuators by harnessing snap-through instabilities

The Harvard community has made this article openly available. [Please share](#) how this access benefits you. Your story matters

Citation	Overvelde, Johannes T. B., Tamara Kloek, Jonas J. A. D'haen, and Katia Bertoldi. 2015. "Amplifying the Response of Soft Actuators by Harnessing Snap-through Instabilities." <i>Proc Natl Acad Sci USA</i> 112 (35) (August 17): 10863–10868. doi:10.1073/pnas.1504947112.
Published Version	doi:10.1073/pnas.1504947112
Citable link	http://nrs.harvard.edu/urn-3:HUL.InstRepos:27657494
Terms of Use	This article was downloaded from Harvard University's DASH repository, and is made available under the terms and conditions applicable to Other Posted Material, as set forth at http://nrs.harvard.edu/urn-3:HUL.InstRepos:dash.current.terms-of-use#LAA

Amplifying the response of soft actuators by harnessing snap-through instabilities

Johannes T. B. Overvelde^a, Tamara Kloek^a, Jonas J. A. D'haen^a, and Katia Bertoldi^{a,b,1}

^aJohn A. Paulson School of Engineering and Applied Sciences, Harvard University, Cambridge, MA 02138; and ^bKavli Institute, Harvard University, Cambridge, MA 02138

Edited by John W. Hutchinson, Harvard University, Cambridge, MA, and approved July 21, 2015 (received for review March 11, 2015)

Soft, inflatable segments are the active elements responsible for the actuation of soft machines and robots. Although current designs of fluidic actuators achieve motion with large amplitudes, they require large amounts of supplied volume, limiting their speed and compactness. To circumvent these limitations, here we embrace instabilities and show that they can be exploited to amplify the response of the system. By combining experimental and numerical tools we design and construct fluidic actuators in which snap-through instabilities are harnessed to generate large motion, high forces, and fast actuation at constant volume. Our study opens avenues for the design of the next generation of soft actuators and robots in which small amounts of volume are sufficient to achieve significant ranges of motion.

soft actuator | snap-through instability | fluidic segment | amplification

The ability of elastomeric materials to undergo large deformation has recently enabled the design of actuators that are inexpensive, easy to fabricate, and only require a single source of pressure for their actuation, and still achieve complex motion (1–5). These unique characteristics have allowed for a variety of innovative applications in areas as diverse as medical devices (6, 7), search and rescue systems (8), and adaptive robots (9–11). However, existing fluidic soft actuators typically show a continuous, quasi-monotonic relation between input and output, so they rely on large amounts of fluid to generate large deformations or exert high forces.

By contrast, it is well known that a variety of elastic instabilities can be triggered in elastomeric films, resulting in sudden and significant geometric changes (12, 13). Such instabilities have traditionally been avoided as they often represent mechanical failure. However, a new trend is emerging in which instabilities are harnessed to enable new functionalities. For example, it has been reported that buckling can be instrumental in the design of stretchable soft electronics (14, 15), and tunable metamaterials (16–18). Moreover, snap-through transitions have been shown to result in instantaneous giant voltage-triggered deformation (19, 20).

Here, we introduce a class of soft actuators comprised of interconnected fluidic segments, and show that snap-through instabilities in these systems can be harnessed to instantaneously trigger large changes in internal pressure, extension, shape, and exerted force. By combining experiments and numerical tools, we developed an approach that enables the design of customizable fluidic actuators for which a small increment in supplied volume (input) is sufficient to trigger large deformations or high forces (output).

Our work is inspired by the well-known two-balloon experiment, in which two identical balloons, inflated to different diameters, are connected to freely exchange air. Instead of the balloons becoming equal in size, for most cases the smaller balloon becomes even smaller and the balloon with the larger diameter further increases in volume (Movie S1). This unexpected behavior originates from the balloons' nonlinear relation between pressure and volume, characterized by a pronounced pressure peak (21, 22). Interestingly, for certain combinations of interconnected balloons, such nonlinear response can result in snap-through instabilities at constant volume, which lead to significant and sudden changes of the membranes' diameters (Figs. S1 and S2). It is straightforward to show analytically that these instabilities can be triggered only if the pressure–volume relation of at least one of the membranes

is characterized by (i) a pronounced initial peak in pressure, (ii) subsequent softening, and (iii) a final steep increase in pressure (*Analytical Exploration: Response of Interconnected Spherical Membranes Upon Inflation*).

Highly Nonlinear Fluidic Segments

To experimentally realize inflatable segments characterized by such a nonlinear pressure–volume relation, we initially fabricated fluidic segments that consist of a soft latex tube of initial length L_{tube} , inner radius $R = 6.35$ mm, and thickness $H = 0.79$ mm. We measured the pressure–volume relation experimentally for three segments with $L_{tube} = 22 - 30$ mm, and found that their response is not affected by their length (Fig. S3). Moreover, the response does not show a final steep increase in pressure. This is because latex has an almost linear behavior, even at large strains.

Next, to construct fluidic segments with a final steep increase in pressure and a response that can be easily tuned and controlled, we enclosed the latex tube by longer and stiffer braids of length L_{braid} (Fig. 1A). It is important to note that the effect of the stiff braids is twofold. First, as $L_{braid} > L_{tube}$, the braids are in a buckled state when connected to the latex tube (Fig. 1B), and therefore apply an axial force, F , to the membrane. Second, at a certain point during inflation when the membrane and the braids come into contact, the overall response of the segments stiffens.

We derived a simple analytical model to predict the effect of L_{braid} and L_{tube} on the nonlinear response of these braided fluidic segments (*Simple Analytical Model to Predict the Response of the Fluidic Segments*). It is interesting to note that our analysis indicates that for a latex tube of given length, shorter braids lower the peak pressure due to larger axial forces (Fig. S4 C and E). Moreover, it also shows that L_{braid} strongly affects the volume at which stiffening occurs. In fact, the shorter the braids, the earlier contact between the braids and the membrane occurs, reducing the amount of supplied volume required to have a steep increase

Significance

Although instabilities have traditionally been avoided as they often represent mechanical failure, here we embrace them to amplify the response of fluidic soft actuators. Besides presenting a robust strategy to trigger snap-through instabilities at constant volume in soft fluidic actuators, we also show that the energy released at the onset of the instabilities can be harnessed to trigger instantaneous and significant changes in internal pressure, extension, shape, and exerted force. Therefore, in stark contrast to previously studied soft fluidic actuators, we demonstrate that by harnessing snap-through instabilities it is possible to design and construct systems with highly controllable nonlinear behavior, in which small amounts of fluid suffice to generate large outputs.

Author contributions: J.T.B.O. and K.B. designed research; J.T.B.O., T.K., and J.J.A.D. performed research; J.T.B.O., T.K., and K.B. analyzed data; and J.T.B.O. and K.B. wrote the paper.

The authors declare no conflict of interest.

This article is a PNAS Direct Submission.

¹To whom correspondence should be addressed. Email: bertoldi@seas.harvard.edu.

This article contains supporting information online at www.pnas.org/lookup/suppl/doi:10.1073/pnas.1504947112/-DCSupplemental.

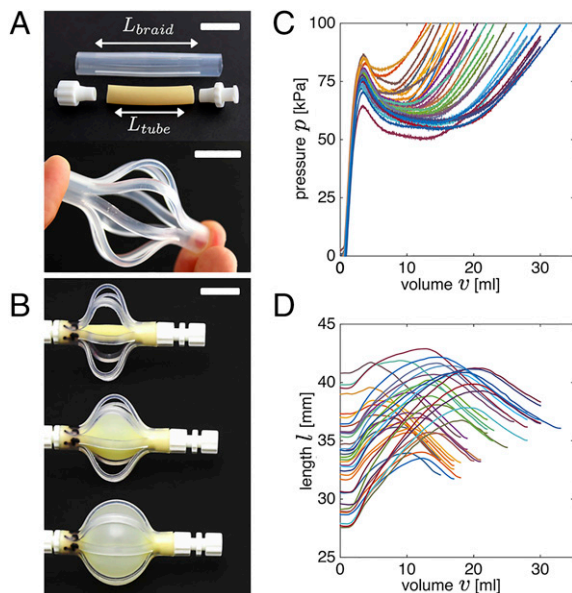


Fig. 1. (A) Outer and stiffer braids are added to the latex tube to create fluidic segments with highly nonlinear response. (B) Snapshots of a segment characterized by $(L_{braid}, L_{tube}) = (46, 20)$ during inflation at $v = 0, 10, 20$ mL. Evolution of (C) pressure (p) and (D) length (l) as a function of the supplied volume (v) for 36 fluidic segments characterized by $L_{braid} = 40 - 50$ mm and $L_{tube} = 20 - 30$ mm. (Scale bars: 10 mm.)

in pressure. Conversely, if L_{braid} is fixed, and the length of the membrane is varied, both the pressure peak and the volume at which stiffening occurs remain unaltered (Fig. S4F). However, in this case we find that shorter tubes lower the pressure of the softening region. Finally, the analytical model also indicates that the length of the fluidic segments, $l = \lambda_z L_{tube}$, initially increases upon inflation (Fig. S4E and F). However, when the tube and braids come into contact, further elongation is restrained by the braids and the segments shorten as a function of the supplied volume.

Having demonstrated analytically that fluidic segments with the desired nonlinear response can be constructed by enclosing a latex tube by longer and stiffer braids, and that their response can be controlled by changing L_{braid} and L_{tube} , we now proceed to fabricate such actuators. The stiffer braids are made from polyethylene-lined ethyl vinyl acetate tubing, with an inner radius of 7.94 mm and a thickness of 1.59 mm. Eight braids are formed by partly cutting this outer tube along its length guided by a 3D printed socket. Finally, Nylon Luer lock couplings (one socket and one plug) are glued to both ends of the fluidic segments to enable easy connection (Fig. 1A). We then measure their response experimentally by inflating them with water at a rate of 60 mL/min, ensuring quasi-static conditions (Fig. 1B and Movie S2).

We fabricated 36 segments with $L_{braid} = 40 - 50$ mm and $L_{tube} = 20 - 30$ mm. As shown in Fig. 1C, all fluidic segments are characterized by the desired nonlinear pressure—volume relation and follow the trends predicted by the analytical model (Fig. S4E and F). In particular, we find that for the 36 tested segments the initial peak in pressure ranges between 65 and 85 kPa (Fig. 1C). We also monitored the length of the segments during inflation (Fig. 1D). As predicted by the analytical model, we find that initially the segments elongate, but then shorten when the tube and braids come into contact. It is important to note that no instabilities are triggered upon inflation of the individual segments, because the supplied volume is controlled, not the pressure.

Combined Soft Actuator

Next, we created a new, combined soft actuator by interconnecting the two segments whose individual response is shown in Fig. 2A. Upon inflation of this combined actuator, very rich behavior

emerges (Fig. 2C and Movie S3). In fact, the pressure—volume response of the combined actuator is not only characterized by two peaks, but the second peak is also accompanied by a significant and instantaneous elongation. This suggests that an instability at constant volume has been triggered.

Numerical Algorithm. To better understand the behavior of such combined actuators, we developed a numerical algorithm that accurately predicts the response of systems containing n segments, based solely on the experimental pressure—volume curves of the individual segments. By using the 36 segments from experiments as building blocks, we can construct $36! / [(36 - n)n!]$ combined actuators comprising n segments (i.e., 630 different combined actuators for $n = 2$; 7,140 for $n = 3$; and 58,905 for $n = 4$), where we assume that the order in which we arrange the segments does not matter. It is therefore crucial to implement a robust algorithm to efficiently scan the range of responses that can be achieved.

We start by noting that, upon inflation, the state of the i th segment is defined by its pressure p_i and volume v_i , and its stored elastic energy can be calculated as

$$E_i(v_i) = \int_{V_i}^{v_i} p_i(\tilde{v}) d\tilde{v}, \quad [1]$$

in which we neglect dynamic effects. Moreover, V_i denotes the volume of the i th segment in the unpressurized state. When the

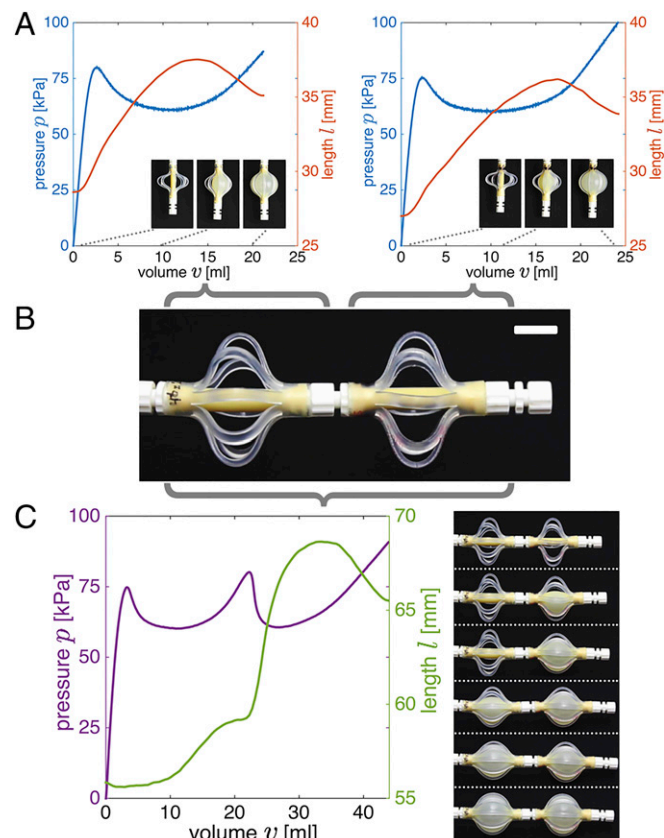


Fig. 2. (A) Evolution of pressure (p) and length (l) as a function of the supplied volume (v) for two fluidic segments characterized by $(L_{braid}, L_{tube}) = (46, 20)$ and $(46, 22)$ mm. Snapshots of the fluidic segments at $v = 0, 10, 20$ and $v = 0, 12, 24$ mL are shown as *Insets*, respectively. (B) The two fluidic segments are connected to form a new, combined soft actuator. (C) Evolution of pressure (p) and length (l) as a function of the supplied volume (v) for the combined actuator. Snapshots of the combined actuator at $v = 0, 9, 18, 27, 36, 45$ mL are shown as *Insets*.

total volume of the system, $v = \sum_{i=1}^n v_i$, is controlled (as in all our experiments), the response of the system is characterized by $n - 1$ variables v_1, \dots, v_{n-1} and the constraint

$$v_n = v - \sum_{i=1}^{n-1} v_i. \quad [2]$$

To determine the equilibrium configurations, we first define the elastic energy, E , stored in the system, which is given by the sum of the elastic energy of the individual segments

$$E(v_1, \dots, v_n) = \sum_{i=1}^n \int_{V_i} p_i(\tilde{v}) d\tilde{v}, \quad [3]$$

and use Eq. 2 to express the energy in terms of $n - 1$ variables

$$\tilde{E}(v_1, \dots, v_{n-1}) = \sum_{i=1}^{n-1} \int_{V_i} p_i(\tilde{v}) d\tilde{v} + \int_{V_n} p_n(\tilde{v}) d\tilde{v}. \quad [4]$$

Next, we implement a numerical algorithm that finds the equilibrium path followed by the actuator upon inflation (i.e., increasing v). Starting from the initial configuration (i.e., $v_i = V_i$), we incrementally increase the total volume of the system (v) and locally minimize the elastic energy (\tilde{E}). Because Eq. 4 already takes into account the volume constraint (Eq. 2), we use an unconstrained optimization algorithm such as the Nelder–Mead simplex algorithm implemented in Matlab (23). Note that this algorithm looks only locally for an energy minimum, similar to what happens in the experiments, and therefore it does not identify additional minima at the same volume that may appear during inflation.

Using the aforementioned algorithm, we find that for many actuators the energy can suddenly decrease upon inflation, indicating that a snap-through instability at constant volume has been triggered. To fully unravel the response of the actuators, we also detect all equilibrium configurations and evaluate their stability. The equilibrium states for the system can be found by imposing

$$\frac{\partial \tilde{E}}{\partial v_i} = 0, \quad \forall i \in \{1, \dots, n-1\}. \quad [5]$$

Substitution of Eq. 4 into Eq. 5, yields

$$\frac{\partial \tilde{E}}{\partial v_i} = p_i(v_i) - p_n \left(v - \sum_{j=1}^{n-1} v_j \right) = 0, \quad [6]$$

$$\forall i \in \{1, \dots, n-1\},$$

which, when substituting Eq. 2, can be rewritten as

$$p_1(v_1) = p_2(v_2) = \dots = p_n(v_n). \quad [7]$$

As expected, Eq. 7 ensures that the pressure is the same in all n segments connected in series.

Operationally, to determine all of the equilibrium configurations of a combined soft actuator comprising n fluidic segments, we first define 1,000 equispaced pressure points between 0 and 100 kPa. Then, for each of the n segments we find all volumes that result in those values of pressure (Fig. S5A). Finally, for each value of pressure, we determine the equilibrium states by making all possible combinations of those volumes (Fig. S5B). Note that by using Eq. 2 we can also determine the total volume in the system at each equilibrium state, and then plot the pressure–volume response for the combined actuator (Fig. S5C).

Finally, we check the stability of each equilibrium configuration. Because an equilibrium state is stable when it corresponds

to a minimum of the elastic energy \tilde{E} defined in Eq. 4, at any stable equilibrium solution the Hessian matrix

$$H(\tilde{E})(v_1, \dots, v_{n-1}) = \begin{bmatrix} \frac{\partial^2 \tilde{E}}{\partial v_1^2} & \dots & \frac{\partial^2 \tilde{E}}{\partial v_1 \partial v_{n-1}} \\ \vdots & \ddots & \vdots \\ \frac{\partial^2 \tilde{E}}{\partial v_{n-1} \partial v_1} & \dots & \frac{\partial^2 \tilde{E}}{\partial v_{n-1}^2} \end{bmatrix} \quad [8]$$

is positive definite. Note that the second-order partial derivatives in Eq. 8 can be evaluated as

$$\frac{\partial^2 \tilde{E}}{\partial v_i \partial v_j} = \begin{cases} p_i'(v_i) + p_n' \left(v - \sum_{k=1}^{n-1} v_k \right), & \text{if } i = j \\ p_n' \left(v - \sum_{k=1}^{n-1} v_k \right), & \text{if } i \neq j, \end{cases} \quad [9]$$

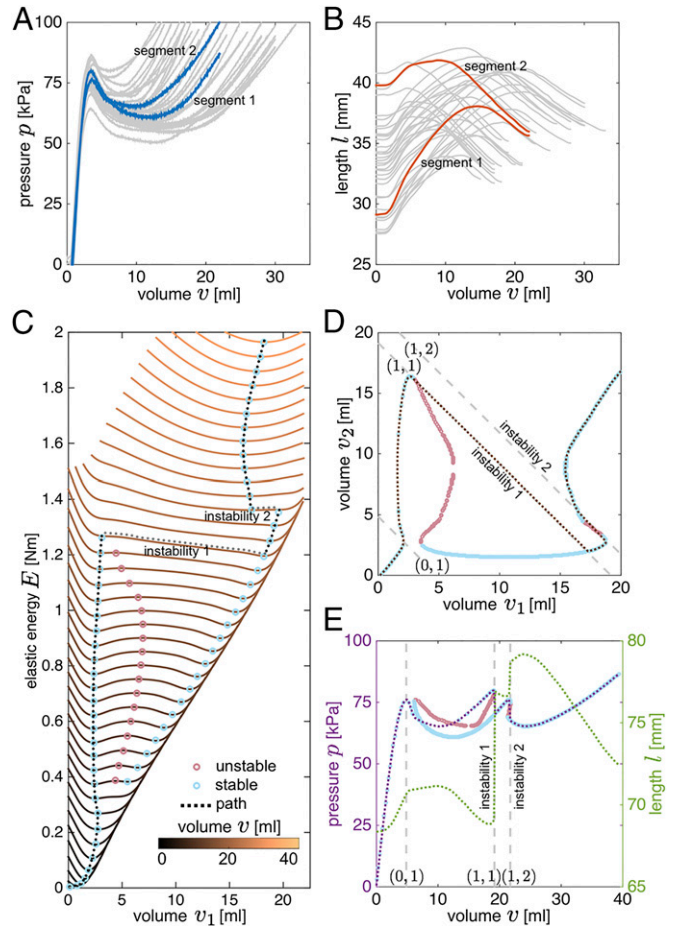


Fig. 3. (A) Experimentally measured pressure–volume relations for all 36 fabricated fluidic segments. (B) Experimentally measured length–volume relations for all 36 fabricated segments. (C) Numerically determined elastic energy, E , for a combined actuator comprising the two segments whose individual behavior is highlighted in A and B. The energy is shown for increasing values of the supplied volume, v . The stable and unstable equilibrium configurations are highlighted by blue and red circular markers, respectively. (D) Equilibrium configurations for the combined actuators. At $v = 19$ mL an unstable (1, 1) transition is found, resulting in a significant internal volume flow. A second instability of type (1, 2) is then triggered at $v = 22$ mL. (E) Numerically determined pressure–volume and length–volume relations for the combined soft actuator.

in which $p'_i(\bar{v}) = dp_i/d\bar{v}$. Taking advantage of the fact that all off-diagonal terms of the Hessian matrix are identical and using Sylvester's criterion (24), we find that an equilibrium state is stable if

$$\prod_{i=1}^k p'_i(v_i) + p'_n \left(v - \sum_{k=1}^{n-1} v_k \right) \sum_{i=1}^k \prod_{j=1, j \neq i}^k p'_j(v_j) > 0, \quad [10]$$

$$\forall k = 1, \dots, n-1.$$

Numerical Results. To demonstrate the numerical algorithm, we focus on two segments where the experimentally measured pressure–volume and length–volume responses are highlighted in Fig. 3A and B. In Fig. 3C we report the evolution of the total elastic energy of the system, E , as a function of the volume of the first segment, v_1 , for increasing values of the total supplied volume, v , and in Fig. 3D we show all equilibrium configurations in the v_1 – v_2 plane. We find that initially ($0 < v < 5$ mL) the volume of both segments increases gradually. However, for $5 < v < 19$ mL, v_1 remains almost constant and all additional volume that is added to the system flows into the second segment. Moreover, at $v = 6$ mL a second local minimum for E emerges, so that for $6 < v < 19$ mL the system is characterized by two stable equilibrium configurations. Although for $v > 13$ mL this second minimum has the lowest energy, the system remains in the original energy valley until $v = 19$ mL. At this point the local minimum of E in which the system is residing disappears, so that its equilibrium configuration becomes unstable, forcing the actuator to snap to the second equilibrium characterized by a lower value of E . Interestingly, this instability triggers a significant internal volume flow from the second to the first segment (Fig. 3D) and a sudden increase in length (Fig. 3E). Further inflating the system to $v = 22$ mL triggers a second instability, at which some volume suddenly flows back from the first to the second segment. After this second instability, increasing the system's volume further inflates both segments simultaneously.

All transitions that take place upon inflation (i.e., at $v = 5, 19$, and 22 mL) are highlighted by a peak in the pressure–volume curve (Fig. 3E), and correspond to instances at which one or more of the individual segments cross their own peak in pressure. These state transitions can either be stable or unstable (Fig. 3C–E). A stable transition always leads to an increase of the elastic energy stored in the system, and an instability results in a new equilibrium configuration with lower energy. Each state transition can therefore be characterized by the elastic energy release, which we define as a normalized scalar $\Delta \hat{E} = (E_{post} - E_{pre})/E_{pre}$. Here and in the following, the subscripts *pre* and *post* indicate the values of the quantity immediately before and after the state transition. Moreover, to better understand the effects of each transition on the system, we

define the associated normalized changes in internal volume distribution, length and pressure as $\Delta \hat{v} = \max(v_{i,post} - v_{i,pre})/V_{pre}$, $\Delta \hat{l} = (l_{post} - l_{pre})/l_{pre}$ and $\Delta \hat{p} = (p_{post} - p_{pre})/p_{pre}$.

In Fig. 4 we report $\Delta \hat{v}$, $\Delta \hat{l}$, and $\Delta \hat{p}$ versus the normalized change in energy, $\Delta \hat{E}$, for all transitions that occur in the 630 combined soft actuators comprising $n = 2$ segments. Note that there are more than 630 data points, because all actuators show two or more state transitions. We find that $-0.1 \leq \Delta \hat{E} \leq 4 \cdot 10^{-5}$, indicating that some of the transitions are stable (i.e., $\Delta \hat{E} > 0$), and others are unstable ($\Delta \hat{E} < 0$). We furthermore observe that the energy increase for stable transitions is very small, and is therefore sensitive to the increment size used in the numerical algorithm. By contrast, the elastic energy released during unstable transitions can be as high as 10% of the stored energy.

We also characterize each state transition according to the changes induced in the individual segments, and use (α, β) to identify the number of segments to the right of their pressure peak before (α) and after (β) the state transition. For combined soft actuators comprising $n = 2$ segments, the numerical results show three possible types of transitions: (0, 1), in which both segments are initially on the left of their peak in pressure and then one of them crosses its pressure peak during the state transition (blue markers in Fig. 4); (1, 2), in which the second segment also crosses its peak in pressure (green markers in Fig. 4); (1, 1), in which both segments cross their pressure peak, but one while inflating and the other while deflating (red markers in Fig. 4). We find that transitions of type (0, 1) occur in all combined actuators and are always stable. Therefore, the associated changes in elastic energy, length, pressure, and the internal volume distribution are approximately zero. By contrast, transitions of type (1, 1) are always unstable and result in both high elastic energy release (up to 10%) and high internal volume flow (up to 80%). Unlike (1, 1), transitions of type (1, 2) can be either stable or unstable. The unstable transitions result in moderate energy release (up to 2.5%), but can lead to significant and instantaneous changes in length (up to 14%). Therefore, our analysis clearly indicates not only that snap-through instabilities at constant volume can be triggered in soft fluidic actuators, but also that the associated released energy can be harnessed to trigger sudden changes in length, drops in pressure, and internal volume flows.

Experimental Results. To validate the numerical predictions, we measured experimentally the response of several combined actuators. In Fig. 5A we show the results for the system whose predicted transitions are indicated by the diamond gray markers in Fig. 4. We compare the numerically predicted and experimentally observed mechanical response, finding an excellent agreement. In particular, for this combined actuator we find that the pressure–volume curve is characterized by two peaks, indicating

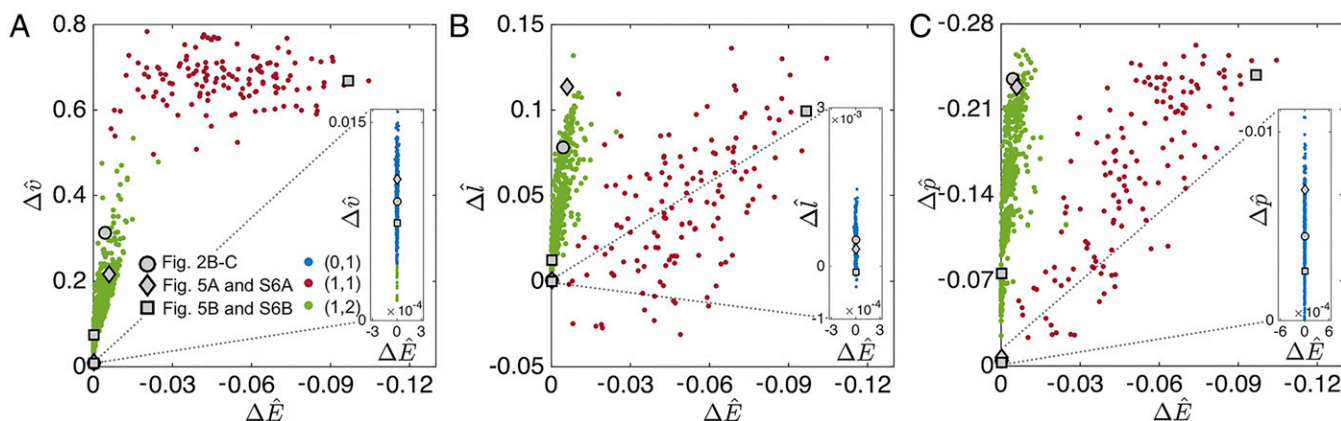


Fig. 4. A–C show $\Delta \hat{v}$, $\Delta \hat{l}$ and $\Delta \hat{p}$ versus the normalized change in energy $\Delta \hat{E}$ for all state transitions that occur in the 630 combined soft actuators comprising $n = 2$ fluidic segments. Blue, red, and green markers correspond to (0, 1), (1, 1), and (1, 2) transitions, respectively; (A) $\Delta \hat{v}$ versus $\Delta \hat{E}$; (B) $\Delta \hat{l}$ versus $\Delta \hat{E}$; and (C) $\Delta \hat{p}$ versus $\Delta \hat{E}$.

result, small compressors are sufficient to inflate these actuators, making them highly suitable for untethered applications.

Our results indicate that by combining fluidic segments with designed nonlinear responses and by embracing their nonlinearities, we can construct actuators capable of large motion, high forces, and fast actuation at constant volume. Although here we have focused specifically on controlling the nonlinear response of fluidic actuators, we believe that our analysis can also be used to enhance the response of other types of actuators (e.g., thermal, electrical and mechanical) by rationally introducing strong nonlinearities. Our approach therefore enables the design of a class of nonlinear systems that is waiting to be explored.

Materials and Methods

All individual soft fluidic segments and combined actuators investigated in this study are tested using a syringe pump (Standard Infuse/Withdraw PHD Ultra; Harvard Apparatus) equipped with two 50-mL syringes that have an accuracy of $\pm 0.1\%$ (1000 series, Hamilton Company). The segments and the combined actuators are inflated at a rate of 60 and 20 mL/min, respectively,

ensuring quasi-static conditions. Moreover, during inflation the pressure is measured using a silicon pressure sensor (MPX5100; Freescale Semiconductor) with a range of 0–100 kPa and an accuracy of $\pm 2.5\%$, which is connected to a data acquisition system (NI USB-6009, National Instruments). The elongation of the actuators is monitored by putting two markers on both ends of each actuator, and recording their position every two seconds with a high-resolution camera (D90 SLR, Nikon). The length of the actuator is then calculated from the pictures using a digital image processing code in Matlab. Each experiment is repeated 5 times, and the final response of the actuator as shown in the paper is determined by averaging the results of the last four tests. Finally, we measured the force exerted by the actuators during inflation when their elongation is completely constrained. In this case we use a uniaxial materials testing machine (model 5544A; Instron, Inc.) with a 100-N load cell to measure the reaction force during inflation.

ACKNOWLEDGMENTS. This work was supported by the Materials Research Science and Engineering Center under National Science Foundation Award DMR-1420570. K.B. also acknowledges support from the National Science Foundation (CMMI-1149456-CAREER) and the Wyss institute through the Seed Grant Program.

1. Laschi C, Mazzolai B, Mattoli V, Cianchetti M, Dario P (2009) Design of a biomimetic robotic octopus arm. *Bioinspir Biomim* 4(1):015006.
2. Ilievski F, Mazzeo AD, Shepherd RF, Chen X, Whitesides GM (2011) Soft robotics for chemists. *Angew Chem Int Ed Engl* 50(8):1890–1895.
3. Mosadegh B, et al. (2014) Pneumatic networks for soft robotics that actuate rapidly. *Adv Funct Mater* 24:2163–2170.
4. Martinez RV, et al. (2013) Robotic tentacles with three-dimensional mobility based on flexible elastomers. *Adv Mater* 25(2):205–212.
5. Martinez RV, Glavan AC, Keplinger C, Oyetibo AI, Whitesides GM (2014) Soft actuators and robots that are resistant to mechanical damage. *Adv Funct Mater* 24:3003–3010.
6. Roche ET, et al. (2014) A bioinspired soft actuated material. *Adv Mater* 26(8):1200–1206.
7. Majidi C (2013) Soft Robotics: A perspective—Current trends and prospects for the future. *Soft Robotics* 1:5–11.
8. Tolley MT, et al. (2014) A resilient, untethered soft robot. *Soft Robotics* 1:213–223.
9. Shepherd RF, et al. (2011) Multigait soft robot. *Proc Natl Acad Sci USA* 108(51):20400–20403.
10. Morin SA, et al. (2012) Camouflage and display for soft machines. *Science* 337(6096):828–832.
11. Kim S, Laschi C, Trimmer B (2013) Soft robotics: A bioinspired evolution in robotics. *Trends Biotechnol* 31(5):287–294.
12. Singamaneni S, Tsukruk V (2010) Buckling instabilities in periodic composite polymeric materials. *Soft Matter* 6:5681–5692.
13. Chen D, Yoon J, Chandra D, Crosby AJ, Hayward RC (2014) Stimuli-responsive buckling mechanics of polymer films. *J Polym Sci, B, Polym Phys* 52:1441–1461.
14. Rogers JA, Someya T, Huang Y (2010) Materials and mechanics for stretchable electronics. *Science* 327(5973):1603–1607.
15. Wang Y, et al. (2011) Super-elastic graphene ripples for flexible strain sensors. *ACS Nano* 5(5):3645–3650.
16. Shim J, Perdigo C, Chen ER, Bertoldi K, Reis PM (2012) Buckling-induced encapsulation of structured elastic shells under pressure. *Proc Natl Acad Sci USA* 109(16):5978–5983.
17. Florijn B, Coulais C, van Hecke M (2014) Programmable mechanical metamaterials. *Phys Rev Lett* 113(17):175503.
18. Wang P, Casadei F, Shan S, Weaver JC, Bertoldi K (2014) Harnessing buckling to design tunable locally resonant acoustic metamaterials. *Phys Rev Lett* 113(1):014301.
19. Keplinger C, Li T, Baumgartner R, Suo Z, Bauer S (2012) Harnessing snap-through instability in soft dielectrics to achieve giant voltage-triggered deformation. *Soft Matter* 8:285–288.
20. Li T, et al. (2013) Giant voltage-induced deformation in dielectric elastomers near the verge of snap-through instability. *J Mech Phys Solids* 61:611–628.
21. Miller JS (1952) Pressure within a bubble. *Am J Phys* 20:115.
22. Merritt DR, Weinhaus F (1978) The pressure curve for a rubber balloon. *Am J Phys* 46:976–977.
23. Lagarias JC, Reeds JA, Wright MH, Wright PE (1998) Convergence properties of the Nelder–Mead simplex method in low dimensions. *SIAM J Optim* 9:112–147.
24. Gilbert GT (1991) Positive definite matrices and Sylvester’s criterion. *Am Math Mon* 98:44–46.
25. Gent AN (1999) Elastic instabilities of inflated rubber shells. *Rubber Chem Technol* 72:263–268.
26. Kanner LM, Horgan CO (2007) Elastic instabilities for strain-stiffening rubber-like spherical and cylindrical thin shells under inflation. *Int J Non-Linear Mech* 42:204–215.
27. Weinhaus F, Barker W (1978) On the equilibrium states of interconnected bubbles or balloons. *Am J Phys* 46:978–982.
28. Dreyer W, Müller I, Strehlow P (1982) A study of equilibria of interconnected balloons. *Q J Mech Appl Math* 35:419–440.
29. Levin Y, da Silveira FL (2004) Two rubber balloons: Phase diagram of air transfer. *Phys Rev E Stat Nonlin Soft Matter Phys* 69(5 Pt 1):051108.
30. Müller I, Strehlow P (2004) *Rubber and Rubber Balloons: Paradigms of Thermodynamics*, Lecture Notes in Physics (Springer, New York).
31. Gent AN (1996) A new constitutive relation for rubber. *Rubber Chem Technol* 69:59–61.
32. Haughton D, Ogden R (1978) On the incremental equations in non-linear elasticity — ii. Bifurcation of pressurized spherical shells. *J Mech Phys Solids* 26:111–138.
33. Ertepinar A (1972) Theoretical and experimental studies on shells of arbitrary wall-thickness subjected to internal and external pressure. Ph.D. dissertation (Drexel University, Philadelphia).
34. Alexander H (1971) Tensile instability of initially spherical balloons. *Int J Eng Sci* 9:151–160.
35. Ogden R (1988) *Non-Linear Elastic Deformations* (Dover, New York).
36. Chater E, Hutchinson JW (1984) On the propagation of bulges and buckles. *J Appl Mech* 51:269–277.
37. Kyriakides S, Yu-Chung C (1990) On the inflation of a long elastic tube in the presence of axial load. *Int J Solids Struct* 26:975–991.
38. Kyriakides S, Yu-Chung C (1991) The initiation and propagation of a localized instability in an inflated elastic tube. *Int J Solids Struct* 27:1085–1111.